Chapter 4

Flow and Transport in Catalytic Reactors

In chemical engineering many processes involve fixed bed (mainly catalytic) reactors and as such, the study of the hydrodynamics and transport phenomena inside these systems is of great interest, and fundamental to their design. Usually, parameters of interest (such as mass transfer or dispersion coefficients) are obtained from the corresponding experimentally validated correlations, or from new experimental investigations. However, due to the geometrical features proper of these reactors, these studies are not at all straightforward: many small-scale complexities may arise, which have a great impact on the overall system behavior, both in the fluid flow and in transport processes. This makes the preparation of comprehensive bench-scale experiments difficult, and results in a challenging scale-up of the results obtained at the small-scale to the larger industrial scale of interest. Moreover, it is very difficult to explore the whole range of variation of the properties of interest, as for example the packed bed porosity, the size distribution of the catalyst particles and their shape. These issues are in fact shared by the larger field of study of flow and transport in random porous media. In this respect, an interesting alternative to experimental investigation is represented by computer simulations via computational fluid dynamics (CFD), which can help in limiting the number of experiments to be conducted and allowing for wider exploration of packing characteristics and operating conditions. Moreover, complex small-scale phenomena can be more deeply investigated, in a way usually not attainable with the use of experiments only. Many works have already demonstrated the effectiveness of this approach in the study of packed bed reactors (Augier et al., 2010a,b).

A modified version of this chapter has been published in Boccardo et al. (2014a)

In order to perform a reliable CFD simulation, the starting point is in the choice of an accurate geometric model representing the actual system, and it being as realistic as possible. As it was introduced in Chap. 3, in this dissertation we have decided to rely on a *in-silico* algorithmic reconstruction of a geometrical model, which faithfully represents the real system in all of its features. As mentioned, this provides for a number of advantages, such as the extremely lower cost of such an approach with respect to using the more sophisticated experimental techniques mentioned, or the easiness of generating and testing a very high number of loading realizations, with varying particle shapes and particle size distributions. Obviously, great care must be given as to ensure that the reconstructed model is accurate both as a purely geometrical description and, perhaps more importantly, in showing the same fluid dynamic behaviour of the real system under investigation.

The objective of this work is therefore to demonstrate the validity of the procedure just described, in both these aspects. First, a procedure for the replication of the catalyst loading process, via computer graphics and ballistic physics simulation, is developed and tested for a number of different catalyst shapes. A validation of the viability of the resulting geometries is performed, involving the comparison of the models void fractions with experimental results. In this way, a number of models representing different packed bed configurations are obtained. Subsequently, for each catalyst shape, the influence of the features of the grain size distribution (i.e.: the variance for Gaussian distributions) on the resulting packing bulk porosity is analyzed. Also, a great deal of attention was paid to the meshing process. Meshes with different levels of refinement were generated, and results concerning the evaluation of the critical cell size necessary to obtain both a good discretization of the grains surface and a precise description of the contact points between them, are shown. CFD simulations are performed on these systems: fluid flow is described by solving the continuity and Navier-Stokes equations. The results, especially regarding pressure drop in the bed, are compared to empirical models of pressure drop in porous media. Eventually, it is interesting to observe that the developed workflow, from geometry and mesh generation, to CFD simulation and post-processing totally relies on free open-source code.

4.1 Test cases and operating conditions

4.1.1 Obtaining the geometric model

As mentioned, the first part of this work deals with the development of a robust tool for effectively simulating the stacking of particles in a packed bed, with particular attention to catalytic particles and catalytic reactors. In order to do that the software `Blender` (Van Gumster, 2009) is used. `Blender` avails of the Bullet Physics Library, which is a large collection of codes used to manage the dynamics of rigid bodies and, most importantly, to detect and calculate the outcome of the collisions between these bodies. This library provides for a number of iterative methods combining accuracy, speed and robustness, enabling for the simulations of a very large number of elements, as it will be shown further on; moreover, a clear advantage of using this code with respect to many other algorithms used to recreate granular media models lies in the possibility to manage any particle shape, even complex non-convex ones, which are the ones of most difficult treatment in rigid body simulations. An additional advantage lies with the fact that `Blender` does not consider the flow of the fluid in-between particles. Being generally this fluid air, its presence has very little influence during the packing process. This makes the use of Blender way more interesting from the computational point of view with respect to other similar codes that instead do account for these effects, such as those based on Discrete Element Methods (DEM). The choice of the code `Blender` was also made due to its extensive scripting functionality. A tool was then developed (in the language Python3) and plugged into the main rigid body simulation code, with the purpose of quickly setting up different simulation cases, with several particle shapes, particle size distributions, total numbers, and containers in which the particles settle. The shapes considered are spheres and cylindrical and trilobe extrudates, while the containers tested were cubes and cylinders. An example of three cylindrical loadings, of spheres, cylinders, and trilobes, can be found in Fig. 4.1.

Since the purpose is to mimic the loading of the catalyst beads into the reactor in a realistic manner, the particles are initially placed on top of the container, with gravity causing their deposition into it, with the end state of the simulation provided by a stable solution of the balance of the forces acting on them, namely gravity and the interaction forces. The choice of the initial placement of the grains in the setup of the rigid body simulation is a step worth discussing. As mentioned, the purpose is to replicate the process of physically filling the reactor with catalyst particles as accurately

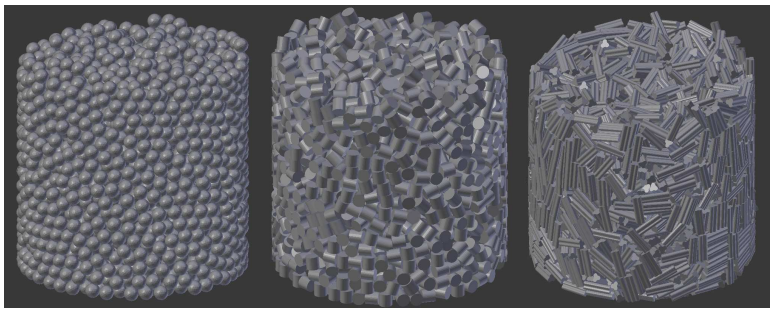

Figure 4.1: Packing of spheres, cylindrical beads, and trilobes in cylindrical containers.

as possible: to that end, different ways of funnelling the particles in the system are devised and tested, and they are shown in Fig. 4.2.

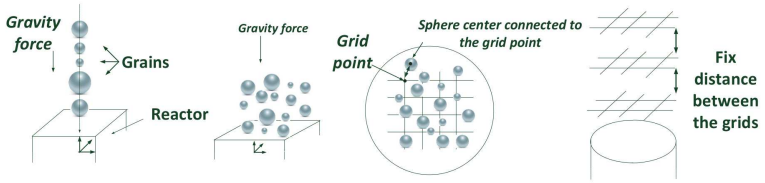

Figure 4.2: Three different types of initial particle placement.

In short, the first way is the simplest to implement but the less realistic one, with every particle falling in the container through a single straight line, while the other two represent the actual process quite well, with the random "grid" placement giving the best results. The difference in the latter lies in the additional step of allowing for a certain distance between the grids, resulting in more time for each set of particle to settle and thus in a more stable simulation. When items which do not possess spherical symmetry are considered, such as cylindrical beads and trilobes, a randomization of their orientation is also added during their placement in the grid.

Two other very important points in the setup of the physical simulation concern the geometric description of the particles during the resolution of the collision events and the mechanical parameters governing their behavior. All particle shapes are represented in Blender with a "watertight" (closed) external mesh, constituted of triangular or quadrangular elements. Hence, the representation of a sphere (for example) will depend on the definition with which the surface is discretized: its refinement level. The higher this refinement level is, the better the model will be but also obviously the heavier

the computational cost for calculating the rigid body dynamics and collision events will be. For example, a sphere with refinement level equal to one is an icosahedron, with each further refinement level splitting each triangular face into four triangles, resulting in a smoother surface. In the results section of this chapter the choice for a suitable trade-off in this matter will be presented and justified. Moreover and even more importantly, a choice has to be made of the collision model of the particle. Many times, in fact, it may not be necessary to use an object surface mesh: in the simple case of a sphere for example, only a two-parameter description (its center and its radius) is necessary to perfectly describe its position and behavior in the physical simulation. The savings in both memory requirements and computational cost with respect to the use of the full surface mesh is evident. There are of course scales of increasing complexity: for an highly non-spherical convex shape the computation of the nearest-approximating convex hull will be needed, and the most complex case is that of a non-convex shape, and the trilobes considered in this work pertain to this category. In this last case, the whole surface mesh will be needed during the rigid body dynamics computation, leading in a more expensive simulation with respect to the case of spheres.

Lastly, the parameters governing the calculation of interactions between the objects have to be considered: the interparticle potential employed is the hard-sphere potential, according to which no interpenetration between each particle is possible, and upon contact a collision occurs. These collisions are governed by the coefficient of restitution and the friction factor. Both of these parameters can be modified, greatly influencing the outcome of the physical simulation. In almost all cases, these settings have been specified in order to replicate the real physical characteristics of the materials involved, but in some cases this was not the most desirable course of action. For the case of trilobes, using the true values for these parameters led to an unrealistic geometric model, showing an excessive packing anisotropy and porosity. In this case, these two parameters are then tuned (reducing the friction factor and increasing the restitution coefficient) in order for the geometrical characteristics of the resulting model to match corresponding validated experimental data. The rationale in this case is to give priority to obtain a realistic and precise simulation result over trying to describe accurately the intermediate deposition and settling steps: the same methodology was followed in Augier et al. (2010a), where a DEM approach was used, in order to improve the density of the loading. Results pertaining this effect and our solution for it will be presented in the next section.

4.1.2 Mesh Generation

After having obtained the geometric models with `Blender` and having validated them, the analysis of the pressure drop through the identified granular beds was conducted. In this work, fluid flow results pertaining to three different geometric models will be presented. The first one is a cubic sample (with sides equal to 1.25 cm) of a packing of uniformly distributed spheres with diameter equal to 1.99 mm. The second model is again a cubic sample, 0.937 cm in side, of a packing of identical cylindrical beads, with both height and diameter equal to 1.31 mm. The last one is a cubic sample, 1.539 cm in side, of a packing of identical trilobes, with circumscribing diameter $D_t = 1.8$ mm (and equivalent diameter $D_g = 1.44$ mm), and length equal to 4.77 mm. These cubic samples are extracted from larger domains in order to avoid wall effects in CFD simulations (due to high porosity at the walls). The size of this samples is accurately chosen in order to have a representative elementary volume (REV) as detailed in the results and discussion section.

A mesh is thus created for these three cases, to be used in the finite volume CFD code. The mesh utility `snappyHexMesh`, included in the open-source package `OpenFOAM` (OpenCFD, 2013), is used. The first step in the meshing process is the creation of a structured, cartesian grid in the entirety of the bounding volume of the system considered. Next, the volume pertaining to the geometric model is subtracted, leaving a cartesian grid in the fluid portion approximating the particles surface with a stair-step description. Finally, the mesh is further modified by moving each boundary vertex, relocating them closer to the original model surface, resulting in a body fitted mesh. The mesh generation process is critical to both obtaining grid independent results during the fluid flow simulation, and for ensuring that the CFD model constitutes a faithful representation of the original geometry. In all the simulations presented in this work, the cell layer next to the surface of the particles underwent an additional refinement step, to account for the sharper momentum boundary layer near the walls and thus adequately describing it. Moreover, a certain level of refinement near the surface of the particles is necessary to give a satisfactory definition of the contact points, which can be wrongly approximated as larger contact solid volumes if too coarse a mesh is employed. An example of this is given in Fig. 4.3.

Moreover, the mesh porosity strictly depends on the dimension of the cells around the grains: an adequate number of cells is needed for the discretized model in the mesh to adequately represent the original model.

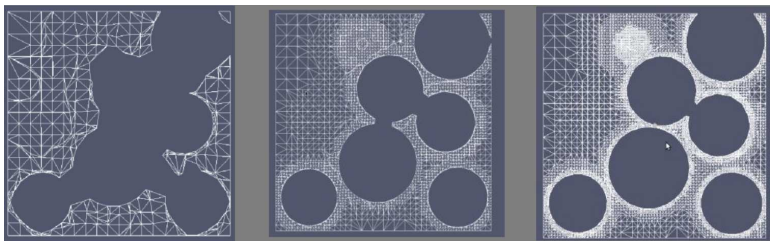

Figure 4.3: Grain surface definition at three increasing mesh refinement levels.

Again, Fig. 4.3 visually clarifies this phenomenon, and in order to quantify this effect a 7 mm sized sample in a larger packing, constituted of a Gaussian distribution of spheres of average diameter equal to 1.99 mm, was analyzed. The porosity of the actual model, result of the `Blender` simulation, is 0.344. Then, several meshes with different cell dimensions are created, and the ratio between the porosity of the meshed sample and the original geometry, $\varepsilon_m/\varepsilon_g$, is calculated. The results are presented in Fig. 4.4.

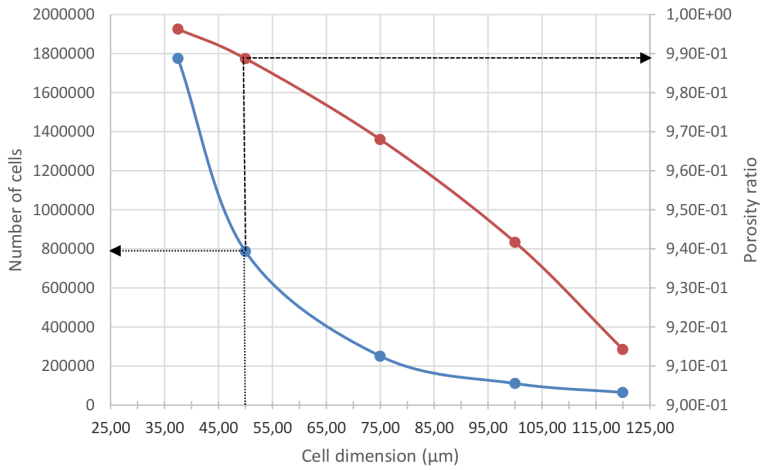

Figure 4.4: Porosity ratio and number of cells versus cell dimension for a spheres packing

As it can be seen, very coarse meshes can result in a very low $\varepsilon_m/\varepsilon_g$ ratio, down to $\varepsilon_m/\varepsilon_g \approx 0.9$, while a grid with mesh cell size of 50 μm (corresponding to 800,000 cells in this sample geometry) leads to $\varepsilon_m/\varepsilon_g \approx 0.99$, which corresponds to a faithful representation of the original model. The acceptable cell dimension obviously depends on the average particle diameter: this result shows that an analysis of this type is a necessary step

during the mesh generation process. The final models after the meshing operation can be seen in Fig. 4.5, while Fig. 4.6 shows a close-up view of the actual mesh for one of them.

Each of the samples is comprised of approximately 300 grains, with the size of the mesh being respectively equal to around 8.5, 11 and 22 million cells. Table 4.1 explains the meshing strategy employed in each case, showing the two different cell dimensions for the "near-grain" zone (four cells thick for all cases) and the volume bulk.

Packing	Bulk cell dimension (μm)	"Near-grain" cell dimension (μm)
Spheres	80	40
Cylinders	52	26
Trilobes	72	36

Table 4.1: Meshing strategy for the three cases considered. Thickness of the "near-grain" layer equal to four refined cells for all cases.

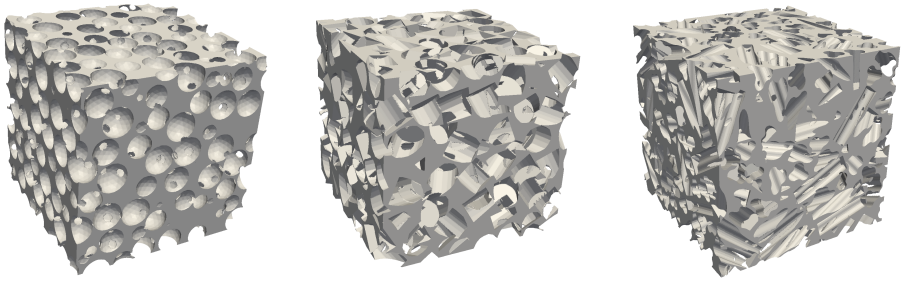

Figure 4.5: Rendering of the final meshed models, respectively for the packing of spheres, cylindrical beads, and trilobes.

4.1.3 Pore-scale CFD simulations

Using the meshes on the cubic samples obtained as described in the previous part, fluid dynamic simulations are performed using the CFD code `OpenFOAM 2.3.0` (some simulations were run with the code `Ansys Fluent 15` for comparison purposes). The fluid velocity field is determined by solving the continuity and Navier-Stokes equations. A no-slip boundary condition is applied on the grain surface. An inlet zone is set on one side of the geometry and an outlet zone at the opposite face, with the fluid entering the domain due to an imposed pressure drop through the medium. No

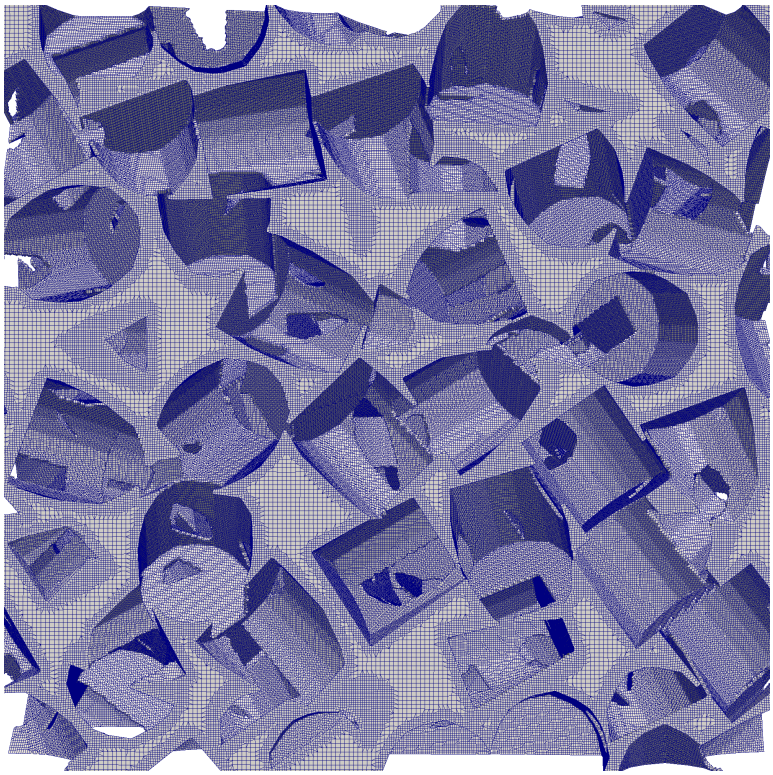

Figure 4.6: View of the final mesh, packing of cylindrical beads.

additional forces (like gravity), are considered. On the remaining sides a condition of symmetry is set, implying no fluid flow across these surfaces, as it is shown in Fig. 4.7. The fluid considered is water, with density $\rho = 997.78$ kg m^{-3} and dynamic viscosity $\mu = 9.768266 \times 10^{-4}$ kg m^{-1}s^{-1}. Thus, the range of operating conditions explored, in terms of Reynolds numbers, is $0.001 < \mathrm{Re} < 0.3$. An overview of the operating conditions of each case for each grain shape can be found in Tab. 4.2. The system is solved for in laminar conditions and under steady-state, with density and viscosity considered constant. The energy equation is not solved.

Having imposed a fixed pressure drop, the data extracted from the simulation results are those relative to the resulting pressure and velocity fields, which are then compared to the predictions from Ergun law, usually employed to describe flow in packed filter beds, reported in Eq. (2.12)

The grain size, D_g used in the calculations in the case of spheres and cylindrical beads is the corresponding Sauter diameter, while for the trilobes it is the calculated equivalent diameter. This value is obtained following the findings of Boyer et al. (2007), where the empirical correlation $D_g =$

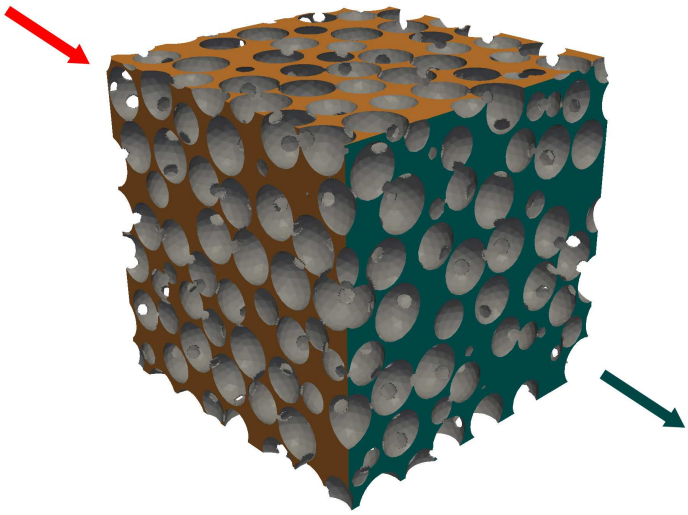

Figure 4.7: Snapshot of the computational domain, with the boundary conditions for the fluid flow in evidence: simmetry boundaries in ochre and the outlet in teal, solid grain walls in grey (inlet zone not pictured). Fluid main direction is indicated by the arrows, red for the inlet, teal for the outlet.

	Spheres	Cylinders	Trilobes
V1	0.7982	2.130	0.648
V2	1.596	4.259	1.297
V3	3.193	8.519	2.593
V4	6.386	17.04	5.187
V5	12.77	34.08	10.37
V6	25.54	68.15	20.75
V7	51.09	238.5	41.49
V8	178.8	834.9	145.2
V9	625.8	2922	508.3
V10	2190	10227	1779
V11	7666	35794	6227
Re	$5.1 \cdot 10^{-3} \div 49$	$2 \cdot 10^{-3} \div 25$	$2.7 \cdot 10^{-3} \div 17$

Table 4.2: Operating conditions for each case, divided by geometry considered (grain shape). Cases V1 through V11 differentiate by imposed pressure drop (in Pa/m in the table, for each case). In the last row, range of Re explored for each case, corresponding to the range of pressure drops reported in the rows above, for each geometry.

C D_t, where D_t is the circumscribing diameter, found to provide the best agreement between the experimental data and Ergun law. The empirical factor C depends on the trilobe size, and is equal to 0.8 in this case.

Grid independence of the CFD results also needed to be ensured: the parameter used to assess this is the equivalent diameter D_g^*. Following a methodology used and described in greater detail in a previous work (Boccardo et al., 2014b) and as described in Chapter 5 of this thesis, each different mesh refinement level is characterized by an effective diameter D_g^*, which is used as a fitting parameter comparing the pressure drop results from steady-state flow simulations at different fluid velocities to the predictions of the Ergun law for that operating conditions. Variations of D_g^* versus cell dimension can then be analysed, and the mesh ensuring grid independent result identified. Results for the case of a packing of Gaussian distributed spheres with an average diameter of 1.99 mm can be found in Fig. 4.8. In this case, a cell dimension of 50 μm will result in a satisfactory discretization of the momentum boundary layer. This result is used in the decision of the appropriate cell dimension for the CFD calculations for all packings, after having taken into due consideration the different dimensions of the grains and as such the need for a different scale of discretization of the properties boundary layers. As already seen, Tab. 4.1 reports the final meshing strategy.

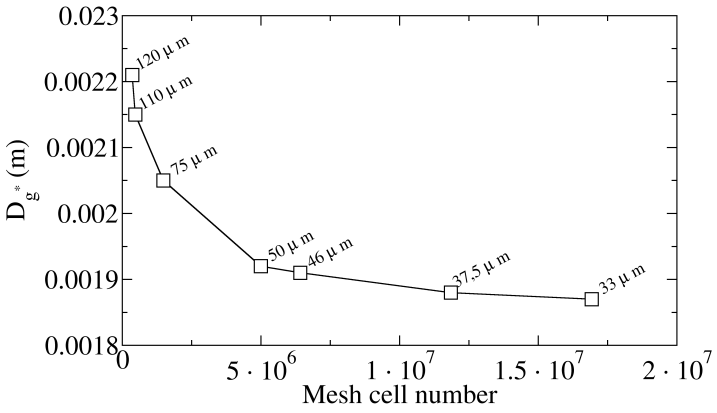

Figure 4.8: Effective grain size, D_g^*, with varying number of mesh cells, and corresponding cell dimension.

4.2 Results and discussion

The purpose of this job is to develop a comprehensive workflow for the performance analysis of catalytic packings fully constituted by open-source simulation tools. In order to do that, both the validity of the geometrical models obtained and the fluid dynamic behaviour of these systems have to be tested. In this section we'll present our results, starting from how a representative elementary volume of the considered media was obtained, and how the geometrical features of the models (bulk and radial porosity) compared with experimental data. Moreover, we analyzed the effect of variations in the distribution variance on the resulting packing bulk porosity. Next, we performed simulations of fluid flow at different conditions in the three types of packing, in order to investigate the pressure drop through these different media. An example of typical flow fields in the packing of spheres, cylindrical beads and trilobes (for one superficial velocity) are shown in Figg. 4.9, 4.10 and 4.11.

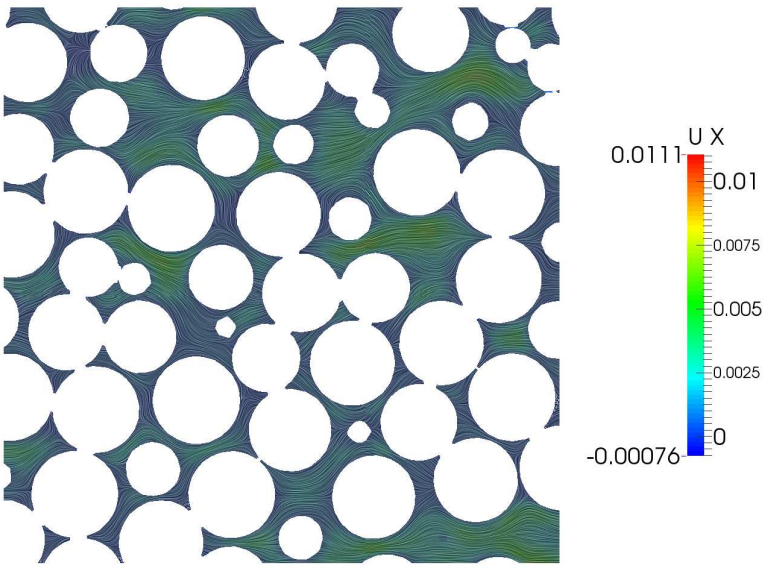

Figure 4.9: Streamlines and contour plot of fluid velocity (in m/s) in a planar cut for the packing of spheres (Re = 1.14). The contour plot refers to the x-component of the fluid velocity, where x is parallel to the main flow direction. Inlet and outlet are on the left and the right side, respectively.

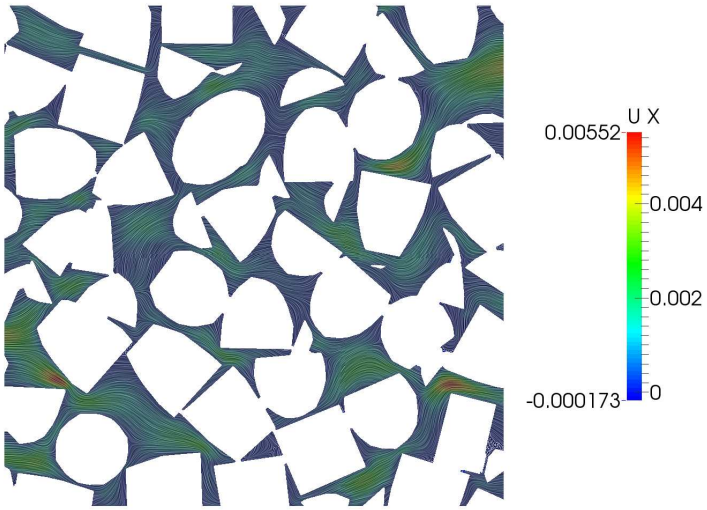

Figure 4.10: Streamlines and contour plot of fluid velocity (in m/s) in a planar cut for the packing of cylindrical beads (Re = 0.28). The contour plot refers to the x-component of the fluid velocity, where x is parallel to the main flow direction. Inlet and outlet are on the left and the right side, respectively.

4.2.1 Geometrical Models Validation

As anticipated, the first test has the purpose of identifying a suitable "size" of the simulation (regarding the total number of grains), in order to quantify the dimension of the smallest representative elementary volume (REV) for the system under investigation. A cubic container, 2.3 cm in size, is filled with 1772 spherical particles, distributed along a Gaussian distribution with an average diameter of 1.99 cm. Cubic samples of different dimensions are taken inside the system, all centered in the center of gravity of the domain, and the corresponding porosity is computed: the results are shown in Fig. 4.12. Three different packings, with spheres meshed at three different refinement levels, are analyzed.

At smaller dimensions, very high porosities are reported: this is expected as for sample sizes of the order of the grains diameter a disproportionately high fraction of a pore or a grain could end up in the sample. At 5 mm and for bigger sizes, the reported porosities reach a stationary value around 0.355, showing another instability arising only with sample sizes of the order of the container size, where wall effects come into play (Zou, 1995). Finding this behavior for this kind of analysis is very satisfactory and equivalent results can be found in other examples in the literature (Bear, 1988). Moreover,

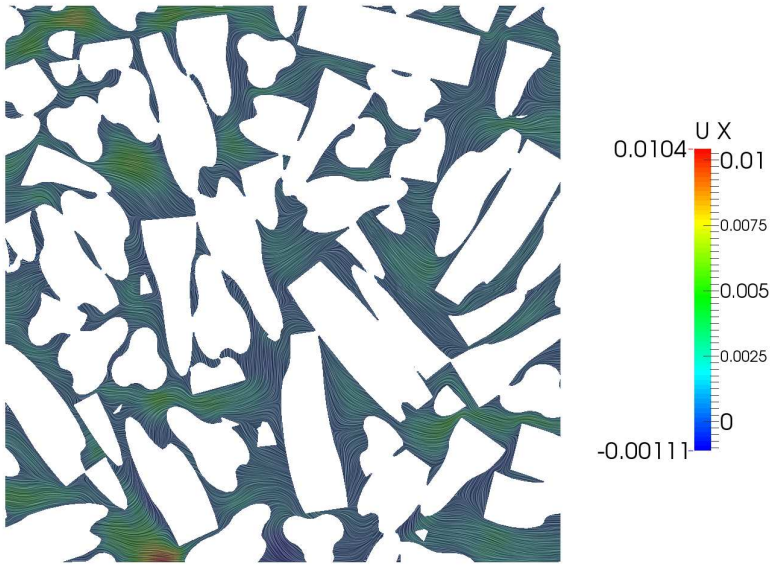

Figure 4.11: Streamlines and contour plot of fluid velocity (in m/s) in a planar cut for the packing of trilobes (Re = 0.60). The contour plot refers to the x-component of the fluid velocity, where x is parallel to the main flow direction. Inlet and outlet are on the left and the right side, respectively.

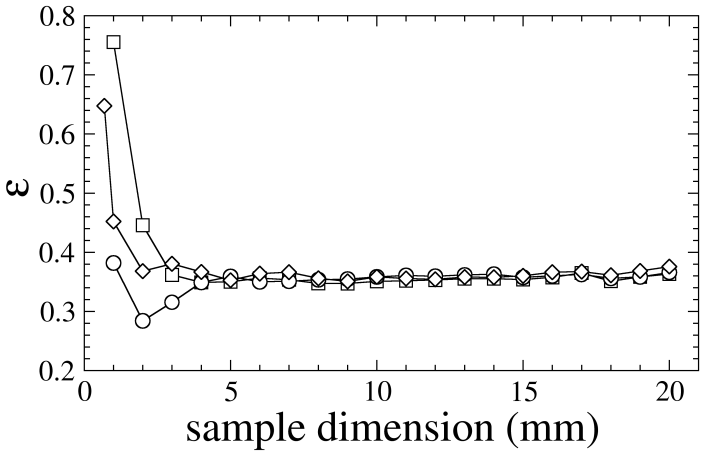

Figure 4.12: Porosity for increasingly large cubic samples, for three different spheres refinement levels (respectively equal to two, three and four surface subdivision levels for circles, squares and diamonds).

this offers an indication for the choice of a refinement level for the particles description: as it can be seen, there are not substantial differences between the three cases except for small sample sizes. What is indicated as refinement level 3 is the most suitable for these applications, as it combines a good representation of the actual shape with an acceptable computational cost during the packing simulation.

Cylindrical containers are also tested, as they resemble the actual reactor shape; moreover, lab-scale experiments are also usually carried out in cylindrical test containers. A polydisperse Gaussian distribution of 4000 particles, with an average diameter equal to 1.99 mm, is loaded with the random grid technique in a series of different containers, as specified in Tab. 4.3. As expected, since the same particle distribution is used in all cases, the results are very close at around $\varepsilon = 0.36$; this result is also in line with data (pertaining to the same particle size) coming from a large experimental campaign dealing with the study of flow conditions in trickle bed reactions (Boyer et al., 2007).

Case	Container		Samples		
	Diameter (cm)	Height (cm)	Diameter (cm)	Height (cm)	ε (-)
P1	3	3	2.9	2.9	0.362
P2	3.5	3	3.35	2.27	0.358
P3	3.7	2.8	3.5	2.2	0.359
P4	4	2.4	3.9	2	0.359

Table 4.3: Porosity for loadings of spherical particles in four different containers, with the corresponding sample dimensions.

For each of the geometries reported in Tab. 4.3 the porosity has been calculated both via averaging a series of 50 cylindrical samples randomly placed in the container (with diameter and height both equal to 5 mm), and via calculating the global packing porosity: the latter is reported in Tab. 4.3. It has to be noted that the dimension of the global sample is slightly lower than that of the container itself: again, this is a necessary precaution in order to avoid the effect of the presence of the walls on this sampling operation, which would markedly affect the porosity reported, with increases of up to one percent.

This wall effect is also more deeply investigated by examining the packing P3 (as referred to in Tab. 4.3). In this case a different sampling strategy is adopted: 200 annular samples, with height equal to 2 cm, are taken. Each of these was placed at the center of the container, and each has a fixed volume

but an increasing diameter, effectively calculating the local porosity value along the radial direction from the center of the packing. The results are shown in Fig. 4.13

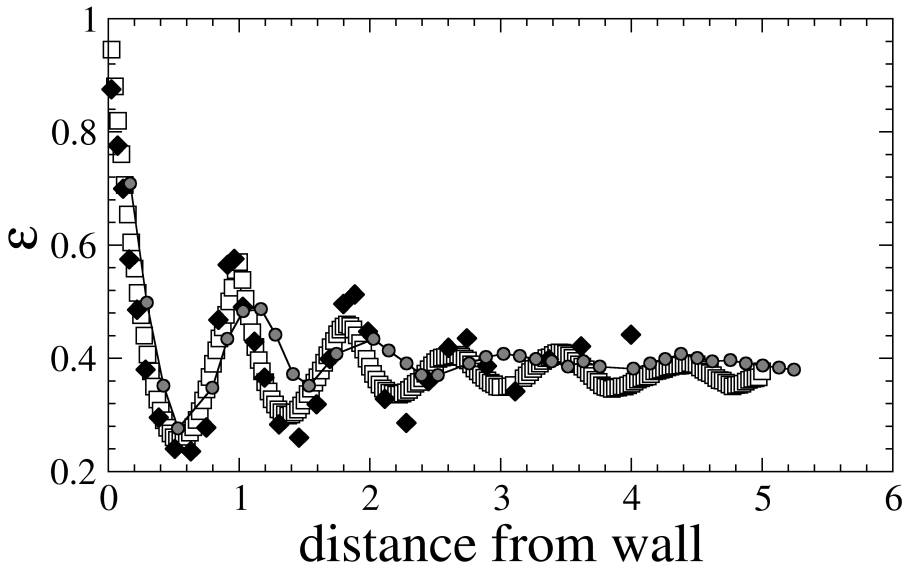

Figure 4.13: Comparison of local porosity values: old packing model (filled circles, Augier et al. (2010a)), current work packing model (white squares) and experimental data (black filled diamonds) for a packing of spheres. Distance from wall expressed in number of equivalent diameters D_g.

In the same figure, these results are compared with two other analyses of the same type: one conducted on an earlier study of an algorithmically generated packing (Augier et al., 2010a), and the other one being actual experimental data (Giese et al., 1998). The accordance between the results obtained in this work and the experimental data is satisfactory, as it confirms that the physical simulation replicates the characteristics of a real packing consistently. The same type of analysis is performed on a packing of uniformly distributed cylinders, and the results are shown in Fig. 4.14, where they are compared with experimental data.

Then, tests are conducted with trilobe packings in cylindrical containers: a Gaussian distribution in length of 3000 trilobes with an average length of 4.77 mm and a circumscribing diameter $D_t = 1.8$ mm (and equivalent diameter $D_g = 1.44$ mm) and standard deviation equal to 1.8 is considered, in a container with diameter and height respectively equal to 3.5 cm and 3

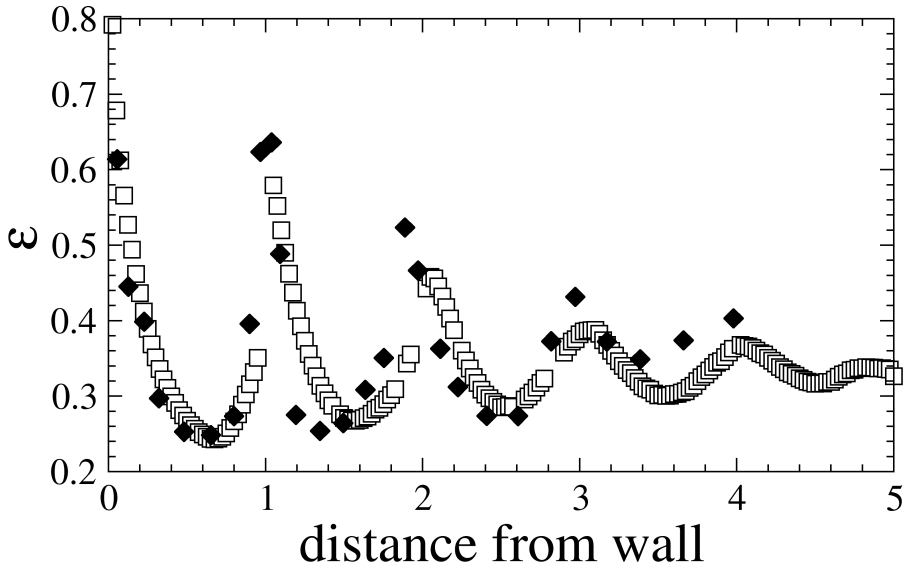

Figure 4.14: Comparison of local porosity values: current work packing model (white squares) and experimental data (black filled diamonds), for a packing of cylindrical beads. Distance from wall expressed in number of equivalent diameters (or equivalently, bead length) D_g.

cm.

As mentioned before, the setup of the physical simulation in the case of the trilobe shape is of the utmost importance, as the resulting loading porosity will vary widely depending on the choice of the bounding volume and of the particular friction factor and coefficient of restitution used. Three simulations comparing different settings of these two parameters are performed, and both the global bed porosity and the porosity distribution inside the bed (using a number of randomly placed samples) are calculated. The results are shown in Tab. 4.4.

Cases	Restitution coefficient	Friction factor	Total ε (-)	Sampled ε (-)
T1	0	0.5	0.415	0.411
T2	0.7	0.325	0.39	0.377
T3	0.85	0.325	0.378	0.364

Table 4.4: Restitution coefficient and friction factor used in three different packing simulations of trilobes, with the resulting total and sampled porosity.

The data reported in this table show how strongly these two physical parameters influence the mixing effect mentioned earlier, and hence the resulting bed porosity. Once again it has to be noted that the total bed porosity is higher than the average porosity calculated through sample averaging, due to the presence of the walls. The difficulties in treating the dynamics of rigid body interactions in the case of such a complex particle shape notwithstanding, it stands to notice that when the right set of collision parameters is used (cases T2 and T3) a remarkable accordance to experimental data was found (Boyer et al., 2007).

Lastly, for each catalytic particle shape, a number of packing realizations (of 3500 grains each) are created, having identical mean particle diameter but differing in the variance of the (Gaussian) grain size distribution. The features of each of the cases considered are found in Tab. 4.5, along with the resulting bulk porosity for each packing. It has to be noted that again, as with the analyses reported in Tab. 4.3, the size of the sample from which the bulk porosity value was obtained is smaller (in the order of two equivalent grain diameters less) than the full container used in the rigid body simulation, in order to remove the effect of the near-wall region on porosity calculations. As expected, there is a slight downward trend in porosity with the increase in the grain distribution non-uniformity both in the case of spherical shape and the cylindrical beads. Instead, in the case of trilobes, increases in the distribution variance seem to have little, if any, effect on the packing porosity. This could be due to either an effect specific of the particular shape considered, or to the much different length/diameter ratio of the trilobe catalyst beads with respect to the cylindrical ones, causing different long range structures in the packing bringing about this unexpected behaviour. This finding calls for deeper investigation, both widening the range of non-uniformity of the distributions, and the aspect ratio of the particle shapes considered.

4.2.2 Fluid Flow Results

The first interesting result can be found in Fig. 4.15, where the pressure profile (for Re = 3.47) for the first geometry (packing of spheres) is shown in comparison with the predictions of Ergun law. The fact that the system shows a linear pressure profile is a good indicator of the validity of the simulated sample chosen, and that can be considered a representative volume for the granular system investigated in this case.

The aggregate results for all the superficial velocities considered can be found in Fig. 4.16, again compared to Ergun law. As it is shown, the CFD

Shape	Case	Characteristic lengths, mm	Standard deviation, mm	ε, -
Spheres	SU1	D_g=1.99	-	0.3775
	SN1		0.15	0.3720
	SN2		0.22	0.3723
	SN3		0.29	0.3678
	SN4		0.36	0.3652
Cyl. beads	CU1	D_g=1.31 L=1.31	-	0.3444
	CN1		0.1	0.3407
	CN2		0.15	0.3413
	CN3		0.19	0.3410
	CN4		0.24	0.3380
Trilobes	TU1	D_g=1.8 L=4.77	-	0.3967
	TN1		0.36	0.4029
	TN2		0.527	0.4029
	TN3		0.695	0.4037
	TN4		0.86	0.4047

Table 4.5: Results of bulk porosity relative to a number of differently distributed packings of spheres, cylindrical beads, and trilobes. Characteristic lengths for each shape are reported: mean diameter in the case of spheres, diameter and average length in the case of cylindrical beads and trilobes. Along, the standard deviation in the distribution (of mean diameter for the spheres and mean length for beads and trilobes) is also reported.

results follow the predictions of the theoretical law within very good margin. This is also the case for the cylindrical beads, where the pressure drop results align on the predictions of Ergun law, as it can be seen in Fig. 4.17. Finally, the same results are obtained for the other geometric model, the packing of trilobes. Again, the pressure profile along the granular medium is linear, exhibiting the same behavior shown in Fig. 4.15. Moreover, Fig. 4.18 shows that even for this complex catalyst shape, the results of the CFD simulations matches the predictions of Ergun law to a very good degree. It is worth mentioning here that the mean grain size used in the Ergun law, reported in Eq. (2.12), was derived in a previous internal study carried out at IFP Energies nouvelles, based on a very large number of experiments. Therefore the agreement between CFD simulations and the Ergun law in this context should be considered as an equivalent validation with experiments.

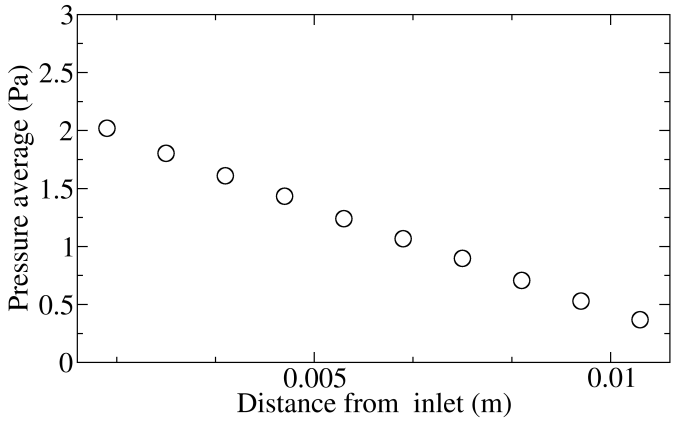

Figure 4.15: Pressure profile inside the granular medium for the packing of spheres, Re = 3.47.

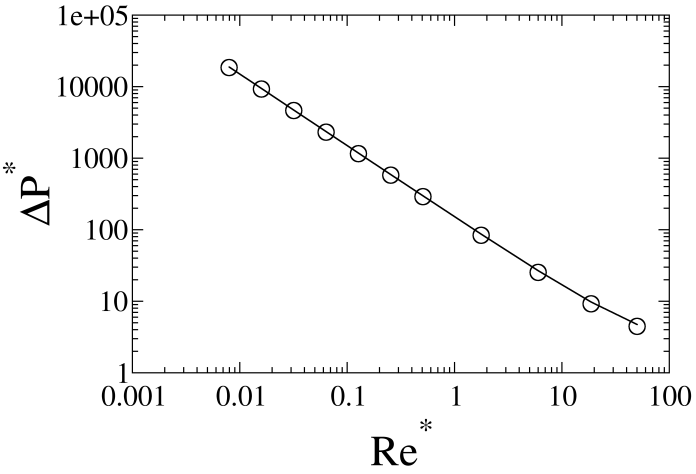

Figure 4.16: Comparison of CFD results (circles) with Ergun's law (continuous line) for the packing of spheres.

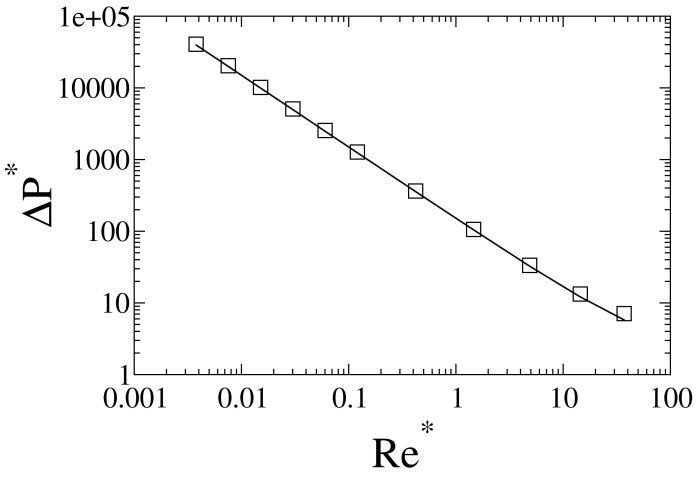

Figure 4.17: Comparison of CFD results (squares) with Ergun's law (continuous line) for the packing of cylindrical beads.

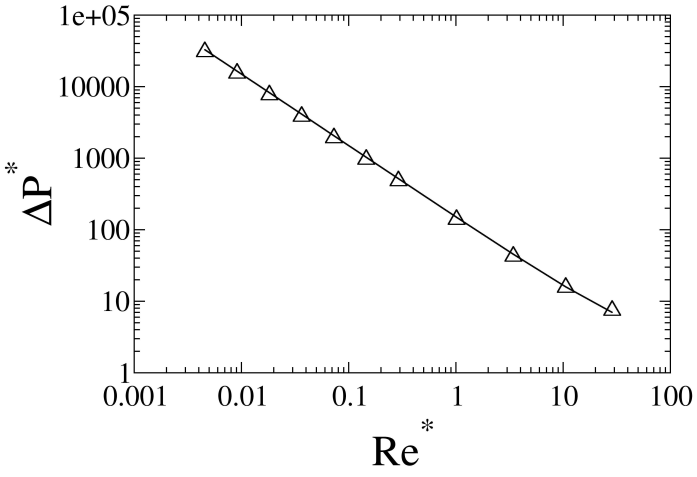

Figure 4.18: Comparison of CFD results (triangles) with Ergun's law (continuous line) for the packing of trilobes.

4.3 Conclusions

In this work a computational tool developed in computer graphics, `Blender`, integrated with the Bullet Physics Library, is used to generate realistic packings of (catalyst) particles of different shapes. The main advantage of this approach (versus other alternatives) stands in the possibility of simulating packings constituted by particles with complex shapes (e.g. non-convex objects such as trilobes).

Results show that attention should be paid to the strategy with which particles are inserted into the container, as well as to the meshing procedure, carried out here with `snappyHexMesh`. The mesh has to be fine enough to describe well the geometrical details of the pores within the packing, as well as the momentum boundary layer around each particle. The validation with experimental data demonstrates that the generated packings realistically describe the behaviour of catalytic fixed bed reactors. In particular, when working with polydisperse spherical particles, the well known radial porosity profiles are obtained, with an accuracy superior to other similar tools. Interesting results are also obtained regarding the influence of the grains polidispersity on the resulting packing bulk porosity, where while for spherical and cylindrical particles the expected inversely proportional relationship is found, this is not true in the case of trilobes. This calls for a deeper investigation, both with regards to the particle shapes considered and to the particle aspect ratio. This last feature especially could be the cause of unexpected packing structures affecting the final bulk porosity value of the packing. Moreover, pressure drop simulations, carried out with `OpenFOAM 2.3.0` show very good agreement with the predictions of the Ergun law (considered "exact" in this context). When working with polydisperse trilobes very good results are also obtained, especially considering that these complex non-convex objects are very difficult to treat. Also in this case comparison between simulated pressure drops and those predicted with the Ergun law (by using a grain size in turn obtained from corresponding experiments) shows an excellent agreement. These results show that the approach developed in this work can be used to more deeply study the effect that the shape, size and length distribution of catalyst particles have on the fluid flow in fixed bed reactors, and improve existing models for pressure drop predictions.